Cite as: J. Alloys Compd. 593, 261 (2014), published version © 2014 Elsevier B.V.
link to published version: http://dx.doi.org/10.1016/j.jallcom.2014.01.034

NMR and Computational Study of $Ba_8Cu_xGe_{46-x}$ Clathrate Semiconductors

Jing-Han Chen[a,*], Ali Sirusi Arvij[a], Xiang Zheng[a], Sergio Y. Rodriguez[a], Joseph H. Ross, Jr.[a]

[a]*Department of Physics and Astronomy, Texas A&M University, College Station, Texas 77843, USA*

Abstract

$Ba_8Cu_xGe_{46-x}$ is a type-I clathrate material that forms as a semiconductor in a narrow composition range corresponding to the electron-balanced Zintl composition, with $x = 5.3$. We use NMR spectroscopy combined with *ab-initio* electronic structure calculations to probe the electronic and structural behavior of these materials. Computational results based on a superstructure model for the atomic configuration of the alloy provide good agreement with the electric quadrupole-broadened NMR lineshapes. Modeling using the modified Becke-Johnson (TB-mBJ) exchange potential is also shown to agree well with experimental NMR Knight shifts. The results indicate that the Cu-Ge balance is the main factor determining the carrier density, within a narrow stability range near the ideal Zintl composition.

Keywords: clathrates, NMR in condensed matter, band structure of semiconductors

1. Introduction

In recent years, clathrates have gained significant attention due to their thermoelectric properties, and potential for device applications [1–10]. Semiconducting clathrates consist of cages of silicon, germanium, or tin in a crystalline framework, with guest atoms located inside the cages. The framework can provide a high Seebeck coefficient (S) and electrical conductivity (σ) while acoustic phonons resonantly scattered from loosely bound guest atoms [11, 12] lead to a very low thermal conductivity (κ). These properties contribute to high values of the thermoelectric figure of merit $ZT = S^2\sigma/\kappa T$. Besides thermal properties, clathrates doped with metal atoms are also interesting for a wide variety of electronic behavior, such as superconductivity and magnetism in Ba_8Si_{46} and related materials [6, 13–15]. Ni- and Au-doped type-I Ba_8Ge_{46} have been found to have metal-to-insulator transitions with varying the concentrations of dopants [16, 17].

In electron microprobe studies copper clathrates with the nominal composition $Ba_8Cu_xGe_{46-x}$ were found to have final compositions [18] in a range close to $x = 5\frac{1}{3}$. This composition balances the electron count in the structural framework [18], with each Ba ion donating 2 electrons to the framework to make up for the electron deficit of Cu vs. Ge. In this way the four-bonded Cu-Ge network maintains four electrons per site needed to fill the valence band, fulfilling what is called the Zintl condition [19]. Johnsen *et al.* [20] examined a series of these materials, and found n-type behavior with samples having composition $x = 6$ exhibiting the lowest carrier density, contrary to the expected Zintl argument. The lowest-n materials also exhibited an unexpected highly resistance behavior, pointing to the possible presence of an impurity band or similar situation involving a large number of scattering centers. One mechanism for this may be the spontaneous occurrence of framework vacancies, which can also help to restore the electron-balance condition [18, 20].

In order to better understand the structural configurations of these materials, and the conditions affecting the transport behavior, we used NMR spectroscopy and electronic structure calculations combined with electron microprobe and crystallographic studies to better understand the band-edge electronic behavior and the corresponding structural properties. Computational analysis included

*Corresponding author. Tel: +1-979-845-7823
Email address: jhchen@tamu.edu (Jing-Han Chen)

the modified Becke-Johnson (TB-mBJ) [21, 22] exchange potential, which was recently shown to provide accurate modeling of semiconductor band-gaps. We find that in computing NMR shifts and relaxation behavior this model also provides good agreement with experiment. Comparing both the wide-line quadrupole NMR spectra and the extracted paramagnetic contributions to the shifts and spin-lattice relaxation times, from computational modeling we find the system to be well-described by a full-framework model, without large numbers of vacancies.

2. Experiment

2.1. Synthesis and Sample Characterization

For initial processing the elemental materials were mixed in stoichiometric quantities, with a small Ba excess included to account for its vapor pressure. Samples were arc melted in argon and then annealed in BN crucibles in evacuated ampoules at 950°C for 3 days, followed by 700°C for 4 days. Three $Ba_8Cu_xGe_{46-x}$ samples were made in this way, with starting compositions $x = 4$, 5.3, and 6. These samples will be designated Cu4, Cu5.3 and Cu6, respectively. Powder x-ray diffraction (XRD) was performed using a Bruker D8 Advance spectrometer, using Cu Kα radiation. Electron microprobe measurements were carried out using wavelength dispersive spectrometry (WDS) methods on a Cameca SX50 equipped with four wavelength-dispersive x-ray spectrometers.

Analysis of the powder XRD room temperature spectra showed characteristic cubic type-I clathrate reflections (space group $Pm\bar{3}n$, with Ba in cage-centered positions). Rietveld refinements were performed using GSAS software [23, 24]. Fig. 1 shows the result obtained for the Cu5.3 sample, while the inset shows the lattice constant vs. starting composition. Small additional reflections were found for unreacted Ge, while Cu6 also exhibited reflections for Cu_3Ge (orthorhombic ϵ_1 phase, consistent with [25], although with large line widths corresponding to considerable strain or other disorder in this phase). The Cu_3Ge fraction in this sample, 0.7 mole ratio per formula unit, corresponds to a fraction 0.30 of the Cu in this sample being found in Cu_3Ge rather than in the clathrate. It has generally been recognized [26] that Cu prefers the 6*c* structural site in the type-I clathrate framework. However because of similar x-ray form factors for Cu and Ge, a precise Cu/Ge ratio and site-occupation parameters can be difficult to obtain with standard powder methods. We found that among the three crystallographic framework sites (6*c*, 16*i*, 24*k*) the fits were made worse for cases of significant Cu occupation of sites other than 6*c*. Therefore for final refinements, Cu occupancy of the other two sites was zeroed out. Cu NMR results shown below provide further confirmation of this result.

The inset of Fig. 1 also shows endpoint values for the series of materials examined in Ref. [20], where synchrotron measurements were used for temperatures up to 273 K, which we extrapolated to 300 K. Lattice constant statistical errors from the powder fits are 0.0001 Å, although within typical systematic uncertainty the results shown with the same starting compositions may be considered to be equivalent.

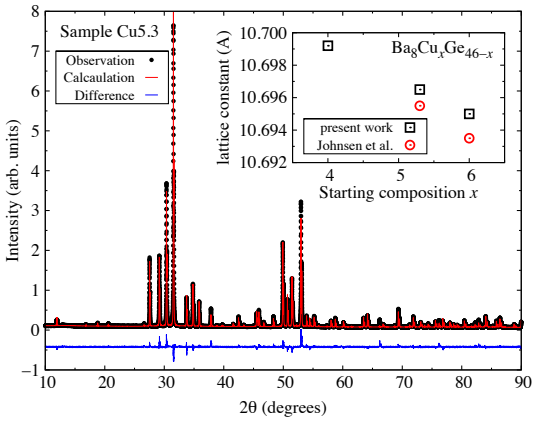

Figure 1: Cu Kα powder x-ray diffraction pattern for Cu5.3 sample, with refinement superposed and difference curve displaced below. Inset shows resulting lattice constants for the three samples, along with extrapolated values from Ref. [20].

WDS measurements showed a minor Cu_3Ge phase in the Cu6 sample, in agreement with XRD, while other samples exhibited only the clathrate phase. Mean values taken at 4 or 5 locations per sample yielded compositions shown in Table 1. These are full-framework atom compositions, and the results were used to obtain final XRD refinements. All compositions correspond to n-type behavior; Table 1 shows the number of excess framework electrons per cell deduced from these compositions, relative to the semiconducting Zintl composition. The uncertainties in n reflect propagation of statistical uncertainties in atom composition (ap-

Table 1: Measured parameters for the samples obtained from WDS microprobe measurements.

site	Ba	Cu	Ge	n/cell
Cu6	7.9	5.26	40.7	0.1±0.1
Cu5.3	7.9	5.19	40.8	0.4±0.2
Cu4	7.7	4.76	41.2	1.5±0.4

proximately 0.1 atom/cell for each case).

Note that for the Cu6 sample composition given in Table 1, assuming that the Cu and Ge remaining from the starting composition formed Ge and Cu_3Ge, we obtain a fraction 0.18 of the Cu being found in Cu_3Ge. This is in rough agreement with the fraction 0.30 obtained from xrd refinement, within uncertainties of the electron microprobe measurement and atomic losses during the arc melting process.

2.2. NMR measurements

NMR experiments were carried out at 77 K and at room temperature using a custom-built pulse spectrometer at fixed field close to 9 T. ^{63}Cu and ^{65}Cu spectra were measured with CuCl solid as standard reference. Powder samples were mixed with crushed quartz to enable rf penetration. Magic angle spinning (MAS) ^{63}Cu NMR measurements were also carried out using a Bruker Advance-400 spectrometer, with solid CuCl as reference.

Fig. 2 shows a broad-line ^{63}Cu spectrum for the Cu5.3 sample. The narrow central line is due to $(1/2, -1/2)$ transitions for the $I = 3/2$ Cu nuclei, while the broad tails are due to satellite transitions dominated by first-order electric quadrupole interactions. The central lines are shown in greater detail in Fig. 3, with the horizontal scale converted to a relative shift. The larger average shift for the Cu4 line is associated with its larger carrier density; its greater line breadth is dominated by the same mechanism. The other two central lines exhibit a structure for which theoretical fits will be described below. A MAS spectrum was also acquired for the Cu6 sample, shown in Fig. 4. Spinning collapses most of the anisotropic shifts, and observation of a single line is additional evidence that Cu occupation is limited to a single site in the parent type-I clathrate structure.

The small peak seen in the wide-line spectrum for Cu6 (Fig. 2 inset) we attribute tentatively to Cu_3Ge (or perhaps one of the two Cu sites in this material). Its shift of about 1360 ppm is outside the typical Cu chemical shift range [27], and must be a metallic shift as would be expected for Cu_3Ge. The integrated intensity for this peak is 0.15 times that of the main central peak, a value that is in line with the powder xrd and extrapolated WDS observations for this sample. This peak could not be narrowed through MAS, consistent with inhomogeneous broadening.

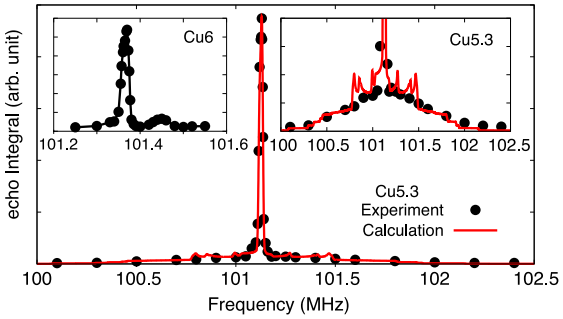

Figure 2: Full quadrupolar ^{63}Cu NMR lineshapes for Cu5.3 sample, with magnified view shown in inset on right. Filled circles: spin echo integration vs. frequency at 77 K. Solid curve: computed spectrum based on 3×1×1 $Ba_8Cu_{5\frac{1}{3}}Ge_{40\frac{2}{3}}$ supercell, and PBE-GGA potential. Left inset: Central portion of Cu6 line shown for comparison.

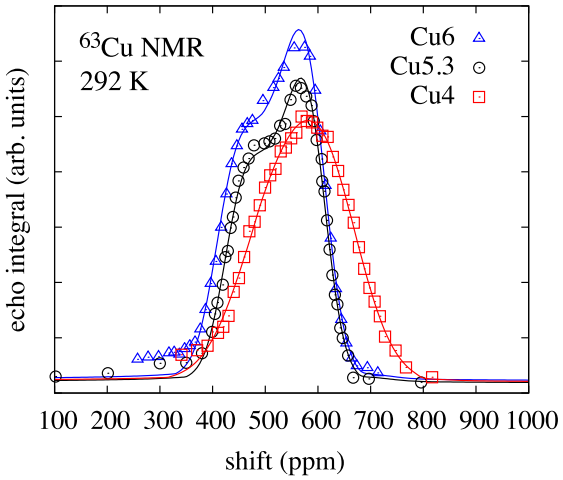

Figure 3: ^{63}Cu central-transition portions of NMR spectra for 3 samples indicated. Solid curves fitted based on $Ba_8Cu_{5\frac{1}{3}}Ge_{40\frac{2}{3}}$ supercell, as described in text.

Measurements of central transition lineshapes and relaxation rates for the two Cu nuclei were used to separate the magnetic and electric quadrupole contributions. For this we used

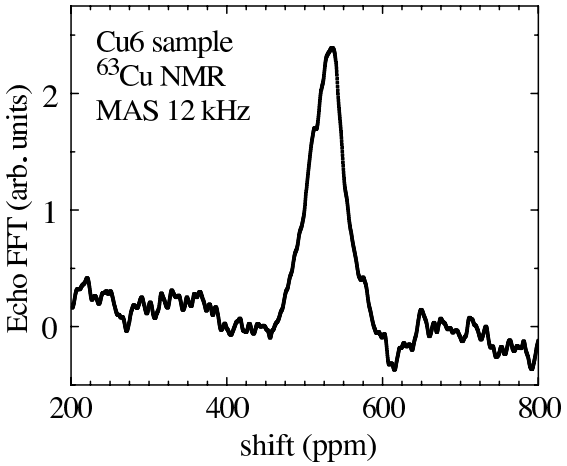

Figure 4: ^{63}Cu MAS spectrum for Cu6 sample.

nuclear moment values reported in Ref. [28] (^{63}Cu, $\gamma = 7.111789/10^7 \mathrm{rad}^{-1}\mathrm{T}^{-1}$ and $Q = 22/\mathrm{fm}^2$. ^{65}Cu, $\gamma = 7.60435/10^7 \mathrm{rad}^{-1}\mathrm{T}^{-1}$ and $Q = 20.4/\mathrm{fm}^2$). The method [29] relies upon magnetic and quadrupole shifts being proportional to γ and Q^2, respectively, where γ is the nuclear gyromagnetic ratio and Q its electric quadrupole moment. A corresponding relationship allows separation of the spin-lattice relaxation rate into magnetic ($1/T_{1M}$) and quadrupolar ($1/T_{1Q}$) components, with the observed rate a sum of these two quantities. The central lineshapes measured at $T = 77$ K and for the ^{65}Cu nucleus do not differ in general features from those shown in Fig. 3, and are not displayed here. Relaxation rates were measured at the points of peak intensity for the central lines.

Center of mass magnetic and quadrupole shifts extracted from the set of lineshape data are shown in Fig. 5(a). Second-order quadrupole effects produce small negative center of mass shifts [30], as observed, and there is little variation between samples in these results. The larger spread in magnetic shift, σ_M, points to Knight shift variations associated with differences in carrier density.

Extracted relaxation rates are shown in Fig. 5(b), multiplied by $1/T$. The observed $1/T_{1Q}$ behavior is consistent with a phonon mechanism, for which $1/T_{1Q}$ rises rapidly vs. T in the vicinity of the Debye temperature [31], as shown schematically by the dashed curve. $1/T_{1M}$ will be driven by free carriers, and this term dominates at all temperatures for the Cu4 sample. For the other two samples $1/T_{1M}$ is much smaller than $1/T_{1Q}$ at room temperature, sufficiently so that the analysis yielded zero as the small $1/T_{1M}$ values could not be reliably extracted relative to the large $1/T_{1Q}$ term. Note that for all of these measurements inversion-recovery data were fitted to the multi-exponential behavior for magnetic central-transition recovery [32]. $1/T_{1Q}$ values hence would require rescaling before quantitative comparison with other materials.

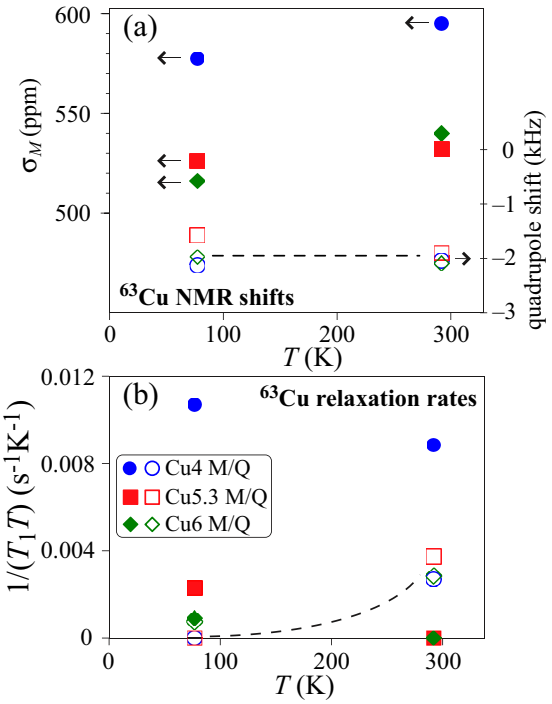

Figure 5: (a) Magnetic (σ_M) and electric quadrupole center of mass ^{63}Cu NMR shifts. (b) Extracted $1/T_{1M}T$ and $1/T_{1Q}T$, computed for ^{63}Cu, samples as indicated. Solid symbols are magnetic (M), open symbols quadrupole (Q), for both plots. Dashed curves connect quadrupole data as guides to the eye.

3. First-principles electronic structures and lineshape modeling

First-principles calculations were performed using the L/APW+lo method [33] as implemented in the WIEN2k code [34]. For these calculations, three configurations were considered: $Ba_8Cu_6Ge_{40}$ with Cu atoms occupying all 6c sites, $Ba_8Cu_5Ge_{41}$ for which one of the 6c sites in each unit cell was occupied by Ge, and $Ba_8Cu_{5\frac{1}{3}}Ge_{40\frac{2}{3}}$, a 3×1×1 superstructure with all 6c sites except two occupied by Ge (Ge on 6c sites chosen to have the same position

in two adjacent cubic cells). The composition of the 3×1×1 superstructure is that of the Zintl phase as described above. For all calculations, the cubic cell size was fixed at the experimental (Cu6 sample) value, and all internal positions were minimized. Calculations were performed with the Generalized Gradient Approximation (GGA) using the widely-used PBE exchange potential [35], and also by using the modified Becke-Johnson (TB-mBJ) [21, 22] exchange potential. 90 k-points were used for 1-cell calculations, while for the 3×1×1 supercell 30 k-points were used.

Fig. 6(a), (b), and (c) show the results of bandstructure calculations for the three configurations, using the TB-mBJ method. The $Cu_{5\frac{1}{3}}$ superstructure (referring here to $Ba_8Cu_{5\frac{1}{3}}Ge_{40\frac{2}{3}}$) is found to be semiconducting, in agreement with the expected Zintl behavior, while Cu_5 and Cu_6 configurations have Fermi levels in the conduction band and valence band, respectively. PBE results (not shown) for the same configurations are qualitatively similar to the TB-mBJ results, but with smaller band-gaps, for example 0.25 eV vs. 0.38 eV for Cu_6, and a very small X-point direct gap of 0.08 eV for $Cu_{5\frac{1}{3}}$ compared to the 0.22 eV gap obtained through TB-mBJ. PBE results for Cu_6 were also reported in Ref. [20], with a similar result as seen here, including the conduction-band minimum at the M point. An Engel-Vosko computation described in the same previous report yielded a somewhat larger gap of 0.52 eV. However the $Cu_{5\frac{1}{3}}$ superstructure exhibits rather different band-edge behavior compared to the parent cubic configurations. Note that the X and M points for the tetragonal supercell are equivalent to X and M points in the simple cubic cell, while A falls on the added zone face in the foreshortened direction in reciprocal space.

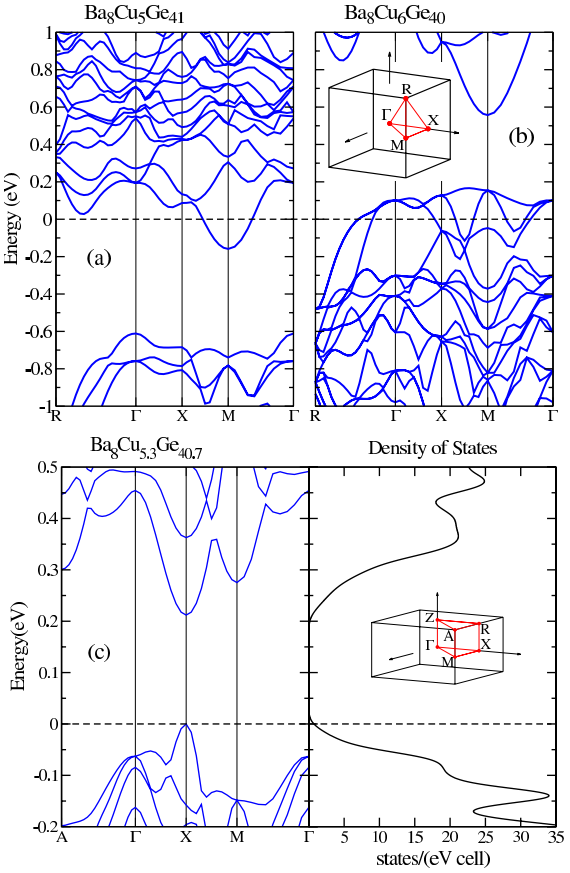

Figure 6: (a) Bandstructure for $Ba_8Cu_5Ge_{41}$ calculated by the TB-mBJ method. (b) $Ba_8Cu_6Ge_{40}$ bandstructure using the same method. Indexing for (a) and (b) according to simple cubic cell, shown in inset. (c) TB-mBJ Bandstructure and total density of states for $Ba_8Cu_{5\frac{1}{3}}Ge_{40\frac{2}{3}}$ $3\times1\times1$ superstructure, with indexing according to tetragonal supercell, lower inset.

Given the very small gap and contrasting conduction-band features for the $Cu_{5\frac{1}{3}}$ superstructure as obtained in PBE, we determined to extend the calculations to include the TB-mBJ computations; TB-mBJ was recently introduced [22, 36] as an improved means for band-gap calculations in semiconductors relative to standard GGA methods. This method has also had success in treatment of other properties relating to the excited states including optical conductivity [37] and thermoelectric behavior [38]. In $Cu_{5\frac{1}{3}}$ the X point band minimum corresponds to 2 degenerate electron pockets, however additional pockets appear in the results starting 0.06−0.08 eV above the band edge. A fit to the density of states in the narrow range 0.22−0.26 eV (with the energy scale of Fig. 6(c)) yielded the approximate effective mass $m^*/m_e = 0.78$ for the lowest pocket (0.49 for each of the two degenerate pockets). A fit over the larger range up to 0.35 eV yielded $m^*/m_e = 1.6$. These results have the same qualitative behavior as previously reported from experiment for n-type samples [20] for which $m^*/m_e = 0.5$ was found in the lowest-carrier density samples, increasing to about 1.1 for larger n. Thus there is general agreement, but with calculated values larger than the reported experimental values by a factor of about 1.5. Note for comparison that effective masses in a series of other direct-gap

semiconductors were previously found to be overestimated [39] by 20-30% using the TB-mBJ method.

The wide-line NMR spectrum (Fig. 2) provides a measure of the distribution of local environments at Cu sites through the first-order influence of local electric field gradients (EFGs), a property of the ground-state electron density. These can also be computed based on *ab-initio* results [40]. Such methods have been shown [41, 42] to provide a good measure of the configuration of other clathrates. Fig. 2 includes a theoretical curve based on the $Cu_{5\frac{1}{3}}$ superstructure, which is in close agreement with the wide-line measurement for the Cu5.3 sample. The amplitude of the NMR central line fixes the vertical scale of the spectrum in the satellite region, and the only other adjustable parameters are a Gaussian broadening width and an overall magnetic shift. These were least-squares fitted to the spectrum using a custom program similar to what was used previously [41, 42]. In the $Cu_{5\frac{1}{3}}$ superstructure the 6*c* positions of the cubic type-I structure are generalized to 6 inequivalent Cu positions, for which the EFG tensors were converted to powder NMR lines, and combined using appropriate multiplicities plus an isotropic shift σ_M, identical for all sites. For these calculations, PBE results were used for consistency with earlier reported results. While the calculated curve exhibits small peaks close to the center that are not apparent in the experimental curve, the overall agreement is very good.

While the TB-mBJ potential has been designed as a method to treat excited states in semiconductors, in some cases the it has been found to provide good agreement for EFG's, which depend upon the ground-state electron density [36]. For comparison we extracted the EFG tensors using mBJ, and found that the values are generally reduced relative to those obtained from PBE. For example in the $Cu_{5\frac{1}{3}}$ superstructure, we found the largest EFG principal value to be reduced by 0.17±0.15 (mean $\pm\sigma$ for the six inequivalent Cu sites), compared to the PBE values. To further compare we ran the $Cu_{5\frac{1}{3}}$ superstructure using the local density approximation (LDA) in WIEN2k, also using the experimental cell with internal positions optimized. The LDA calculation yielded EFG values reduced by only 0.06±0.11, closer to the PBE results.

A further test is provided by fitting the NMR central lines, such as plotted in Fig. 3. These are dominated by second-order quadrupole shifts. Among the measured lines, those for the Cu5.3 and Cu6 samples are nearly identical, while the Cu4 sample exhibits a greater magnetic broadening. Fig. 3 includes theoretical curves showing the agreement between the first-principles EFGs obtained for the $Cu_{5\frac{1}{3}}$ superstructure and the resonance lines for all three samples. For this fit, PBE calculated EFGs were used, the same as for the wideline quadrupole fit of Fig. 2. In order to fit the observed asymmetry a small axial magnetic shift (again identical for each inequivalent site) was included in addition to the isotropic shift. The twelve measured central lines (three samples for two nuclei and two temperatures) were combined with the magnetic shifts plus a Gaussian broadening function, using calculated second-order shapes determined [41, 42] by the computed EFGs for the $Cu_{5\frac{1}{3}}$ superstructure. The resulting isotropic σ_M values are very close to those obtained from the center of mass integration (Fig. 5(a)). These results provide further indication that the filled-framework $Cu_{5\frac{1}{3}}$ supercell model is a good approximation for these materials.

To address energetic stability of the Zintl phase, we determined formation energies from the computed difference between the total energies for each minimized structure and for the equivalent amount of elemental constituents in crystal form. Lattice parameters from the literature were used for each element. Resulting $Ba_8Cu_xGe_{46-x}$ formation energies per formula unit in the PBE model are -10.27 eV for Cu_5, -11.04 eV for $Cu_{5\frac{1}{3}}$, and -12.02 eV for Cu_6. The Cu_6 composition is also lowest in the TB-mBJ model, with a formation energy -19.28 eV/formula unit. There is no deep energy minimum appearing in these results for the Zintl composition, $x = 5\frac{1}{3}$, despite the clear preference for compositions close to this value. Spontaneous vacancies can further adjust the charge balance [18, 20], however the NMR fits are consistent with a full-framework configuration without large numbers of vacancies, so this seems unlikely as an explanation for the stability. Since computed $E(x)$ values have positive curvature it is possible that the clear preference for the $Cu_{5.33}$ phase is due to competition with other phases.

To further analyze the results relative to the simple Zintl picture, in which the system is stabilized by ionic charge transfer from the cations to the framework, we used the quantum theory of atoms in molecules (QTAIM) [43]. This formalism addresses bonding and charge transfer through the

Table 2: Calculated bond critical point charge densities and Laplacians for $Ba_8Cu_6Ge_{40}$. Units: $e/Å^2$, $e/Å^4$

bond	ρ	$\nabla^2\rho$
Cu6*c*-Ge24*k*	0.048	0.056
Ba2*a*-Ge16*i*	0.015	0.033
Ba2*a*-Ge24*k*	0.012	0.025
Ba6*d*-Ge24*k*	0.011	0.023
Ge24*k*-Ge24*k*	0.058	-0.018
Ge16*i*-Ge24*k*	0.063	-0.028
Ge16*i*-Ge16*i*	0.068	-0.042

computed electronic charge density, $\rho(r)$. Table 2 shows all identified bond critical points, which are saddle points in ρ joining neighboring atoms. The results are based on $Ba_8Cu_6Ge_{40}$ in PBE. Negative critical-point values of $\nabla^2\rho$ imply charge localization transverse to the paths joining neighboring atoms, and hence the presence of a directional bond. This is the situation for all of the Ge-Ge bonds, while in contrast all critical points involving Cu and Ba have positive values of $\nabla^2\rho$, a condition normally observed in situations where closed-shell bonding is involved [44].

To further delineate the results we used the CRITIC package [45] for topological analysis of solid state electron densities, using results from WIEN2k as input. Table 3 shows resulting basin charges for the 5 sites. The charge within the QTAIM basin provides a good measure of the actual charge associated with each site [44], and the question of possible bonding of the cage-center Ba has been of general interest because of the connection to rattling behavior. The results show small negative charges for all framework sites, indicating that charge transfer from Ba to Cu and Ge framework sites is nearly uniform. In light of the small Cu-Ge charge difference it appears that the weak Cu bond critical point should be interpreted as weakly metallic, and therefore the Cu sites can be viewed as centers of delocalized charge within the otherwise strongly bonded framework. The large positive charge on Ba and critical point values in Table 2 are consistent with ionic bonding for Ba, although by contrast larger Ba charges near +1.75 electrons were found in an analysis [46] of type-I $Ba_8Ga_{16}Ge_{30}$. These results indicate that in the BaCuGe clathrate as compared with $Ba_8Ga_{16}Ge_{30}$ the cations exhibit less pronounced ionic bonding, and the bonding of the framework itself is more diffuse.

Table 3: Basin charges around different sites from QTAIM model for $Ba_8Cu_6Ge_{40}$.

Site	Basin charge (e)	Site	Basin charge (e)
Ba2*a*	1.21	Ge16*i*	-0.19
Ba6*d*	1.40	Ge24*k*	-0.33
Cu6*c*	-0.14		

4. Analysis and discussion

At 77 K, where the magnetic contribution to $1/T_1$ could be separated for all three samples, both σ_M and $1/T_{1M}$ decrease as the carrier density decreases, as expected for metallic carriers near a band edge. The magnetic shift can be partitioned as $\sigma_M \equiv \sigma_c + K$, where K is the paramagnetic Knight shift due to charge carrier susceptibility, and σ_c is the chemical shift due to other susceptibility contributions. We made the reasonable assumption that σ_c is the same for all compositions, so that variations in σ_M are due to K. Further assuming K to obey a Korringa relation for noninteracting electrons [30], we obtain

$$(\sigma_M - \sigma_c)^2 = \frac{\kappa}{T_{1M}T} = \frac{1}{T_{1M}T}\frac{\hbar\gamma_e^2}{4\pi k_B \gamma_n^2}, \qquad (1)$$

where κ is the Korringa constant, with $\gamma_{n(e)}$ corresponding to the nuclear (electron) gyromagnetic ratio. From a fit of $(\sigma_M - \sigma_c)^2$ vs. $1/(T_{1M}T)$ to a straight line we obtained $\sigma_c = 475$ ppm and thereby $K^2T_{1M}T$, plotted in Fig. 7, was obtained. For this calculation σ_M values from the analytical fitting were used. Note that using the model-independent center of mass integrated values (Fig. 5(a)) gives similar results, for example $\sigma_c = 487$ ppm. $K^2T_{1M}T$ values are consistent with each other, although reduced by about 75% relative to the nominal κ value shown in the figure.

The assumption of metallic behavior is appropriate given the carrier densities in Table 1. For example for the Cu5.3 sample, using the computed $m^*/m_e = 1.6$, we obtain $T_f = 1260$ K. Only for the Cu6 sample does T_f approach room temperature. Thus all samples should be in the metallic regime at 77 K, and for the case of weak interactions the Korringa product should be close to the theoretical value [47], κ. On the other hand in P-doped Si above the metal insulator transition, the Si NMR Korringa product was also observed to have a reduced value. An explanation has been provided in terms of partial occupation of an impurity band [48]. In this case partial localization modifies the carrier dynamics so as to enhance $1/T_1$ to a greater

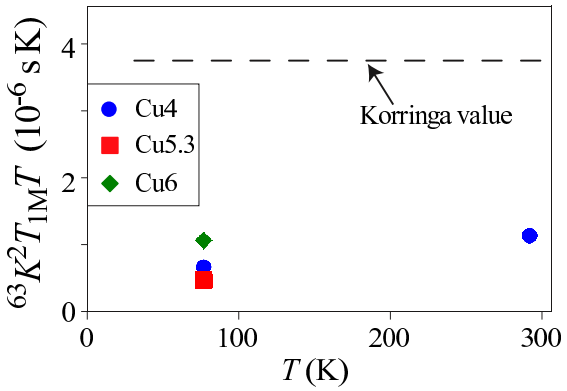

Figure 7: K^2T_1T product based on ^{63}Cu Knight shift (^{63}K) and magnetic contribution to T_1, extracted as described in the text.

extent than any enhancement of K, and $K^2T_{1M}T$ is reduced. Nearness to metal-insulator behavior was also evidenced in previously-reported transport results [20] for low-carrier-density $Ba_8Cu_xGe_{46-x}$ samples for which carrier densities would suggest a normal metallic regime.

From the carrier densities and first-principles electronic structure calculations we can also calculate theoretical Knight shifts. To do so we obtain the total Fermi-level density of states in an effective mass approximation, $g_{tot}(E_f) = (3n/\pi^4)/(m^*\hbar)^2$. The Pauli paramagnetic susceptibility is proportional to this quantity, and correspondingly the Knight shift is given by [30]

$$K = \mu_B g_{tot}(E_f) B_{HF} (g_s/g_{tot}), \qquad (2)$$

where B_{HF} is the hyperfine field, and g_s/g_{tot} represents the ratio of electronic state density in the relevant atomic orbital (s in this case) to the total. For nonmagnetic Cu, the s-contact hyperfine field will far outweigh other contributions, and we used the atomic-based [30] B_{HF} = 260 T. The WIEN2k package divides electronic states into those associated with atomic spheres and interstitial regions. As a means to identify g_s/g_{tot} we computed the ratio using only those states within the spheres. This yields the result of the inset of Fig. 8, based on the TB-mBJ $Cu_{5\frac{1}{3}}$ supercell model, with energies corresponding to Fig. 6(c) so that the plot starts at the conduction-band edge. In the region 0.2-0.4 eV, a small and nearly constant Cu-s contribution $g_s/g_{tot} \approx 0.0014$ is found, as a weighted mean of inequivalent Cu sites in the superstructure. We used this value to calculate the shifts shown in the main plot of Fig. 8. This calculation is valid for the Cu6 and Cu5.3 samples, for which the estimated carrier densities place E_f in the range 0.2−0.3 eV; for the Cu4 sample the estimated carrier density places E_f near 0.45 eV, where additional bands cross (Fig. 6(c)) and g_s/g_{tot} rises (Fig. 8), which seems to account for the larger experimental value in that case. Therefore this model, connecting the Knight shifts to the carrier densities extracted from framework occupation as in Table 1, is successful in reproducing the experimental shifts.

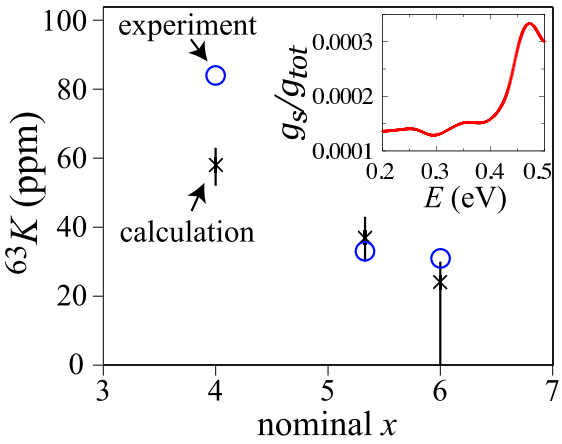

Figure 8: Calculated vs. experimental ^{63}Cu paramagnetic Knight shifts. Inset: Cu-s vs. total density of states ratio as defined in the text.

5. Summary

In summary, we confirmed that $Ba_8Cu_xGe_{46-x}$ ingots with nominal compositions in the range x = 4 to 6 result in compositions close to the $x = 5\frac{1}{3}$ Zintl composition, although first-principles calculations did not indicate a strong energy minimum associated with the semiconducting composition. NMR wide-line and central-transition results both gave very good agreement with analytically-calculated lineshapes based on a 3×1×1 superstructure model for the $x = 5\frac{1}{3}$ composition. Computations based on the TB-mBJ model were also in general agreement with previously reported effective mass results from electrical transport. Separating the quadrupole and magnetic contributions to the NMR shifts and relaxation rates, we obtained an estimate of the chemical shift, and thereby extracted the Korringa behavior. Based on these results we

found good agreement between the observed paramagnetic shifts and estimates based on the computed conduction-band electronic properties.

Acknowledgement

This work was supported by the Robert A. Welch Foundation, Grant No. A-1526, and by the Texas A&M Supercomputing Facility (http://sc.tamu.edu/). We acknowledge helpful discussions with Dr. Nattamai Bhuvanesh.

[1] G. S. Nolas, J. L. Cohn, G. A. Slack, and S. B. Schujman, Appl. Phys. Lett. **73**, 178 (1998).
[2] J. L. Cohn, G. S. Nolas, V. Fessatidis, T. H. Metcalf, and G. A. Slack, Phys. Rev. Lett. **82**, 779 (1999).
[3] V. L. Kuznetsov, L. A. Kuznetsova, A. E. Kaliazin, and D. M. Rowe, J. Appl. Phys. **87**, 7871 (2000).
[4] B. C. Chakoumakos, B. C. Sales, D. G. Mandrus, and G. S. Nolas, J. Alloys Compd. **80**, 296 (2000).
[5] J. Martin, H. Wang, and G. S. Nolas, Appl. Phys. Lett. **92**, 222110 (2008).
[6] J. H. Ross, Jr and Y. Li, in *Nanoscale Magnetic Materials and Applications*, edited by J. P. Liu, E. Fullerton, O. Gutfleisch, and D. Sellmyer (Springer, New York, 2009), chap. 4, p. 105.
[7] H. Zhang, J.-T. Zhao, M.-B. Tang, Z.-Y. Man, H.-H. Chen, and X.-X. Yang, J. Alloys Compd. **476**, 1 (2009).
[8] V. V. Novikov, A. V. Matovnikov, D. V. Avdashchenko, N. V. Mitroshenkov, E. Dikarev, S. Takamizawa, M. A. Kirsanova, and A. V. Shevelkov, J. Alloys Compd. **520**, 174 (2012).
[9] I. Ishii, Y. Suetomi, T. K. Fujita, K. Suekuni, T. Tanaka, T. Takabatake, T. Suzuki, and M. A. Avila, Phys. Rev. B **85**, 085101 (2012).
[10] J. Fulmer, O. I. Lebedev, V. V. Roddatis, D. C. Kaseman, S. Sen, J.-A. Dolyniuk, K. Lee, A. V. Olenev, and K. Kovnir, J. Am. Chem. Soc. **135**, 12313 (2013).
[11] J. S. Tse and M. A. White, J. Phys. Chem. **92**, 5006 (1988).
[12] J. Dong, O. F. Sankey, and C. W. Myles, Phys. Rev. Lett. **86**, 2361 (2001).
[13] S. Yamanaka, E. Enishi, and H. Fukuoka, Inorg. Chem. **39**, 56 (2000).
[14] Y. Li, Y. Liu, N. Chen, G. Cao, Z. Feng, and J. H. Ross, Jr., Phys. Lett. A **345**, 398 (2005).
[15] Y. Li, R. Zhang, Y. Liu, N. Chen, Z. P. Luo, X. Ma, G. Cao, Z. S. Feng, C.-R. Hu, and J. H. Ross, Jr., Phys. Rev. B **75**, 054513 (2007).
[16] S. Johnsen, A. Bentien, G. K. H. Madsen, M. Nygren, and B. B. Iversen, Phys. Rev. B **76**, 245126 (2007).
[17] H. Zhang, H. Borrmann, N. Oeschler, C. Candolfi, W. Schnelle, M. Schmidt, U. Burkhardt, M. Baitinger, J.-T. Zhao, and Y. Grin, Inorg. Chem. **50**, 1250 (2011).
[18] Y. Li, J. Chi, W. Gou, S. Khandekar, and J. H. Ross, Jr., J. Phys.: Condens. Matter **15**, 5535 (2003).
[19] S. M. Kauzlarich, ed., *Chemistry, Structure, and Bonding of Zintl Phases and Ions* (Wiley-VCH, 1996).
[20] S. Johnsen, A. Bentien, G. K. H. Madsen, B. B. Iversen, and M. Nygren, Chem. Mater. **18**, 4633 (2006).
[21] A. D. Becke and E. R. Johnson, J. Chem. Phys. **124**, 221101 (2006).
[22] F. Tran and P. Blaha, Phys. Rev. Lett. **102**, 226401 (2009).
[23] A. C. Larson and R. B. V. Dreele, Los Alamos National Laboratory Report LAUR pp. 86–748 (1994).
[24] B. H. Toby, J. Appl. Cryst. **34**, 210 (2001).
[25] E. Caspi, H. Shaked, H. Pinto, M. Melamud, Z. Hu, O. Chmaissem, S. Short, and J. Jorgensen, J. Alloys Compd. **271–273**, 378 (1998).
[26] G. Cordier and P. Woll, J. Less Common Met. **169**, 291 (1991).
[27] H. Günther, *NMR Spectroscopy: Basic Principles, Concepts and Applications in Chemistry* (Wiley-VCH, Siegen, Germany, 2013), 3rd ed.
[28] R. K. Harris and E. D. Becker, J. Magn. Reson. **156**, 323 (2002).
[29] X. Zheng, S. Y. Rodriguez, and J. H. Ross, Jr., Phys. Rev. B **84**, 024303 (2011).
[30] G. Carter, L. Bennett, and D. Kahan, Prog. Mater. Sci. **20**, 1 (1977).
[31] R. L. Mieher, Phys. Rev. **125**, 1537 (1962).
[32] E. R. Andrew and D. P. Tunstall, Proc. Phys. Soc. **78**, 1 (1961).
[33] G. K. H. Madsen, P. Blaha, K. Schwarz, E. Sjostedt, and L. Nordstrom, Phys. Rev. B **64**, 195134 (2001).
[34] K. Schwarz and P. Blaha, Comp. Mater. Science **28**, 259 (2003).
[35] J. P. Perdew, K. Burke, and M. Ernzerhof, Phys. Rev. Lett. **77**, 3865 (1996).
[36] D. Koller, F. Tran, and P. Blaha, Phys. Rev. B **83**, 195134 (2011).
[37] D. J. Singh, S. S. A. Seo, and H. N. Lee, Phys. Rev. B **82**, 180103 (2010).
[38] J. J. Pulikkotil, D. J. Singh, S. Auluck, M. Saravanan, D. K. Misra, A. Dhar, and R. C. Budhani, Phys. Rev. B **86**, 155204 (2012).
[39] Y.-S. Kim, M. Marsman, G. Kresse, F. Tran, and P. Blaha, Phys. Rev. B **82**, 205212 (2010).
[40] P. Blaha, K. Schwarz, and P. Herzig, Phys. Rev. Lett. **54**, 1192 (1985).
[41] W. Gou, S. Y. Rodriguez, Y. Li, and J. H. Ross, Jr., Phys. Rev. B **80**, 144108 (2009).
[42] S. Y. Rodriguez, X. Zheng, L. Saribaev, and J. H. Ross, Jr., Proc. Mater. Res. Soc. **1267**, DD04 (2010).
[43] R. F. W. Bader, *Atoms in Molecules: A Quantum Theory* (Oxford University Press, USA, 1994).
[44] C. F. Matta and R. J. Boyd, *The Quantum Theory of Atoms in Molecules* (Wiley-VCH, 2007).
[45] A. Otero-de-la-Roza, M. A. Blanco, A. M. Pendás, and V. Luaña, Comput. Phys. Commun. **180**, 157 (2009).
[46] C. Gatti, L. Bertini, N. P. Blake, and B. B. Iversen, Chem. Eur. J. **9**, 4556 (2003).
[47] M. J. R. Hoch and D. F. Holcomb, Phys. Rev. B **71**, 035115 (2005).
[48] E. M. Meintjes, J. Danielson, and W. W. Warren, Jr., Phys. Rev. B **71**, 035114 (2005).